RESOLVING THE BRIGHT HCN(1−0) EMISSION TOWARD THE SEYFERT 2 NUCLEUS OF M51: SHOCK ENHANCEMENT BY RADIO JETS AND WEAK MASING BY INFRARED PUMPING?

SATOKI MATSUSHITA[1], DINH-V- TRUNG[2], FRÉDÉRIC BOONE[3,4], MELANIE KRIPS[5], JEREMY LIM[6], AND SEBASTIEN MULLER[7]

[1] Academia Sinica Institute of Astronomy and Astrophysics, P.O. Box 23-141, Taipei 10617, Taiwan, Republic of China
[2] Institute of Physics, Vietnamese Academy of Science & Technology, 10, Daotan, BaDinh, Hanoi, Vietnam
[3] Université de Toulouse, UPS-OMP, IRAP, F-31400 Toulouse, France
[4] CNRS, IRAP, 9 Av. Colonel Roche, BP 44346, F-31028 Toulouse Cedex 4, France
[5] Institute de Radio Astronomie Millimétrique, 300 Rue de la Piscine, F-38406 Saint Martin d'Hères, France
[6] Department of Physics, University of Hong Kong, Pokfulam Road, Hong Kong
[7] Department of Earth and Space Sciences, Chalmers University of Technology, Onsala Space Observatory, SE-43992 Onsala, Sweden

ABSTRACT

We present high angular resolution observations of the HCN(1–0) emission (at $\sim 1''$ or ~ 34 pc), together with CO $J = 1$–0, 2–1, and 3–2 observations, toward the Seyfert 2 nucleus of M51 (NGC 5194). The overall HCN(1–0) distribution and kinematics are very similar to that of the CO lines, which have been indicated as the jet-entrained molecular gas in our past observations. In addition, high HCN(1–0)/CO(1–0) brightness temperature ratio of about unity is observed along the jets, similar to that observed at the shocked molecular gas in our Galaxy. These results strongly indicate that both diffuse and dense gases are entrained by the jets and outflowing from the active galactic nucleus. The channel map of HCN(1–0) at the systemic velocity shows a strong emission right at the nucleus, where no obvious emission has been detected in the CO lines. The HCN(1–0)/CO(1–0) brightness temperature ratio at this region reaches >2, a value that cannot be explained considering standard physical/chemical conditions. Based on our calculations, we suggest infrared pumping and possibly weak HCN masing, but still requiring an enhanced HCN abundance for the cause of this high ratio. This suggests the presence of a compact dense obscuring molecular gas in front of the nucleus of M51, which remains unresolved at our $\sim 1''$ (~ 34 pc) resolution, and consistent with the Seyfert 2 classification picture.

Key words: galaxies: individual (M51, NGC 5194) – galaxies: ISM – galaxies: jets – galaxies: nuclei – galaxies: Seyfert – ISM: jets and outflows

1. INTRODUCTION

Active galactic nuclei (AGNs) are generally believed to consist of supermassive black holes surrounded by dense material (i.e., molecular gas and dust) in a disk or a torus configuration (e.g., Antonucci 1993). At spatial scales of >100 pc, a number of observations toward nearby AGN host galaxies in molecular gas have uncovered strong concentrations of dense molecular gas at the location of AGNs (e.g., Kohno et al. 2001, 2008a), and these nuclear components often show smooth velocity gradients, suggestive of rotating disks or tori around AGNs (e.g., Jackson et al. 1993; Kohno et al. 1996; Hsieh et al. 2008; Hicks et al. 2009; Sani et al. 2012).

At finer spatial scales of ~ 10 pc, however, molecular gas observations toward some of the previously observed AGNs revealed very different images from the past results observed at larger spatial scales. The nuclear molecular gas shows very disturbed features, such as jet-entrained or outflowing motions from AGNs (Matsushita et al. 2007; Krips et al. 2011; Combes et al. 2013; García-Burillo et al. 2014) or infalling motions toward AGNs (Davies et al. 2009; Müller Sánchez et al. 2009), with little evidence of obscuring rotating disks or tori at this spatial scale. Where is the obscuring material? In this paper, we target one of the nearest Seyfert galaxies, M51 (NGC 5194), to tackle these questions.

M51 hosts a Seyfert 2 nucleus (Ho et al. 1997) with a pair of radio jets (Ford et al. 1985; Crane & van der Hulst 1992). It is located at a distance of 7.1 Mpc (Takáts & Vinkó 2006), which is about one half that of NGC 1068 (14.4 Mpc; Tully 1988), and therefore a very suitable target to observe nuclear molecular gas that requires very high *linear* resolution. The molecular gas around the nucleus of M51 is dense ($>10^4$ cm^{-3}; Kohno et al. 1996) and warm (>100 K; Matsushita et al. 1998, 2004). The molecular gas distribution and kinematics within $\sim 1''$ (~ 34 pc) from the AGN are complex, showing no clear evidence for a disk or torus, but instead two separated features located at the eastern and western sides of the nucleus (Matsushita et al. 2007). The western clump shows a velocity gradient along the radio jets, and its value matches well with that of the ionized gas along the jets (Bradley et al. 2004), strongly indicating that the western clump is entrained by the jets and outflowing from the nucleus (Matsushita et al. 2007).

These previous $\sim 1''$ resolution studies, however, have only been done with CO lines, which might trace different gas components, including diffuse molecular gas, and may confuse our view of the gas distribution and kinematics close to the nucleus. On the other hand, previous $\sim 4''$ resolution HCN(1–0) image (Kohno et al. 1996, 2008b) is not high resolution enough to resolve the detailed structures that have been resolved with the $\sim 1''$ CO observations. In addition, Aalto et al. (2012) reported an HCN(1–0) emission enhancement in the molecular outflows of Mrk 231 at a scale of about 1 kpc, suggesting that the HCN emission can be a good tool for tracing outflows. Observations toward the nucleus of M51 using the HCN(1–0) line at $1''$ or better resolution are therefore essential to understand the physical and chemical interactions between molecular gas and AGN jets. Here, we present $\sim 1''$ resolution HCN(1–0), HCO$^+$(1–0), and HNC(1–0) data toward the nuclear region of M51, together with the $\lesssim 1''$ resolution CO (1–0), (2–1), and (3–2) data, and compare the distributions and kinematics of

these lines. We then discuss the possible emission mechanism of the HCN line from the nuclear region of M51.

2. OBSERVATION AND DATA REDUCTION

2.1. PdBI Observations

We observed the HCN(1–0), HCO$^+$(1–0), and HNC(1–0) lines simultaneously toward the nuclear region of M51 using the IRAM Plateau de Bure Interferometer (PdBI). The array was in the A configuration, and the observation was carried out on 2009 February 1. The system temperatures in the single side band were in the range 80–400 K, depending mostly on the elevation angle (i.e., atmospheric absorption). Three 160 MHz ($\sim$535 km s^{-1}) bandwidth correlators were configured to cover each line. Five 320 MHz units were configured primarily to cover nearby line-free frequencies for continuum observations and calibrations. MWC 349 was observed for the flux calibration, the strong quasar 3C273 was used for the bandpass calibration, and the quasars J1310+323 and J1419+543 were used for the phase and amplitude calibrations. The uncertainty in the absolute flux scale is estimated to be around 5%.

The data were calibrated using GILDAS, and were imaged using AIPS. We did not detect any significant emission for the HCO$^+$(1–0) and HNC(1–0) lines with the 3σ upper limit of 2.0 mJy beam^{-1} in each 20 km s^{-1} channel for both lines within the velocity range of 350–550 km s^{-1}. We also did not detect any continuum emission at 90 GHz with the 3σ upper limit of 0.87 mJy beam^{-1}.

2.2. SMA Observations

The CO(3–2) line was observed with the Submillimeter Array (SMA; Ho et al. 2004)[8] The observation was performed on 2005 April 18, and six out of eight 6 m antennas were used in the extended configuration. The correlator was configured to a 2 GHz bandwidth with a 0.8125 MHz channel resolution, and the line was located at the upper side band. Titan was observed as a flux calibrator, and Uranus, Ganymede, 3C279, and 3C345 were used as bandpass calibrators. J1153+495 and 3C345 were observed every $\sim$20 minutes for the phase and amplitude calibrations. The uncertainty in the absolute flux scale is estimated to be around 15%.

The data calibrations were done using the software package MIR, adapted for SMA[9] This extended configuration data set was combined with the previous compact configuration data set (Matsushita et al. 2004) in the uv plane. The combined data were CLEANed and the images were produced using AIPS.

2.3. Matching uv Ranges

In this paper, we compare the newly obtained HCN(1–0) and CO(3–2) data with the previously obtained PdBI A configuration CO(1–0) data (Matsushita et al. 2007) in various ways, including line ratios. For this purpose, we need to match the shortest uv lengths and the beam sizes of all the data sets, so that they all sample the same structures (i.e., the same spatial frequency components obtained by interferometers). Note that matching the beam size has the same effect as matching the longest uv lengths. The shortest uv length common to all data sets is

imposed by the CO(1–0) data, for which the shortest uv length is 37 kλ (i.e., we can image the structure smaller than $\sim$6$''$). We then convolved all the images to the largest beam size among our data of 1$\farcs$10 $\times$ 0$\farcs$85 with the position angle (P.A.) of 31$°$. We note here that this uv range matching does not significantly change the images from the uv unlimited ones. We did not match the uv range for the CO(2–1) data, since there is a small overlap in the uv range with other data (i.e., CO J = 2–1 data have the shortest uv length twice longer than that of J = 1–0 data, since those data are taken simultaneously with PdBI). As we will show, the CO(2–1) line traces the same features, and is shown for reference, although it is not included in the line ratio calculations.

3. RESULTS

In Figure 1, we show the central $\pm3''$ ($\pm$100 pc) region integrated intensity maps of the CO(1–0), CO(2–1), CO(3–2), and HCN(1–0) lines. All the data except CO(2–1) are uv and beam matched images as mentioned above. The spatial resolution in CO(2–1) is more than a factor of two higher than other images (Matsushita et al. 2007), and is shown here for reference. All the images appear to have similar overall molecular gas distributions and kinematics. There are two clumps located at the western and eastern sides of the nucleus (hereafter clumps S1 and S2, respectively; see Figure 1(a)), whereby western clumps S1 are elongated along the north-south direction. The intensity-weighted velocity maps for all the lines are shown in Figure 2. In all the maps, eastern clump S2 shows increasingly higher blueshifted velocities toward the nucleus, and the western clump S1 shows clear velocity gradient in the north-south direction, as was previously reported by Matsushita et al. (2007). The similarity in the kinematics for all the lines suggests that the overall molecular gas distribution and kinematics at the central $\pm3''$ does not depend on the molecular species (both CO and HCN) or properties (both diffuse and dense gas, and from lower-J to higher-J lines). As mentioned in Section 1, the S1 clump is the jet-entrained molecular gas, so that the similarity of the distribution and kinematics between the CO and HCN data strongly indicates that the both diffuse and dense molecular gas is entrained by the jets and outflowing from the AGN.

With a detailed inspection of the channel maps, however, a distinct difference between the CO and HCN distributions can be seen in a channel map at the systemic velocity (471.7 $\pm$ 0.3 km s^{-1} Shetty et al. 2007). Figure 3 displays three channel maps centered at the velocity of 460, 480, and 500 km s^{-1}, each with a width of $\sim$20 km s^{-1}. In the channel maps at the velocity of 460 and 500 km s^{-1} (i.e., adjacent to the channel at the systemic velocity), all the lines show the emission peaks at either or both eastern and western sides of the nucleus (some emissions elongate toward the nucleus, but do not peak there). On the other hand, in the channel maps at the velocity of 480 km s^{-1}, which includes the systemic velocity of 471.7 $\pm$ 0.3 km s^{-1}, the HCN(1–0) line clearly exhibits a $\sim$5σ peak at the nucleus, where CO lines show no peak if any detectable emission at the nucleus. To further confirm this systemic velocity HCN emission peak, we plot the spectra toward the nucleus of M51 for all four lines in Figure 4. As can be seen, all the CO lines exhibit at best emission at the $\sim$2σ level, but the HCN(1–0) line shows a $\sim$5σ peak only at the systemic velocity channel of 480 km s^{-1}. This therefore indicates that the central HCN(1–0) emission is highly related to the molecular gas around the systemic velocity.

---

[8] The Submillimeter Array is a joint project between the Smithsonian Astrophysical Observatory and the Academia Sinica Institute of Astronomy and Astrophysics, and is funded by the Smithsonian Institution and the Academia Sinica.
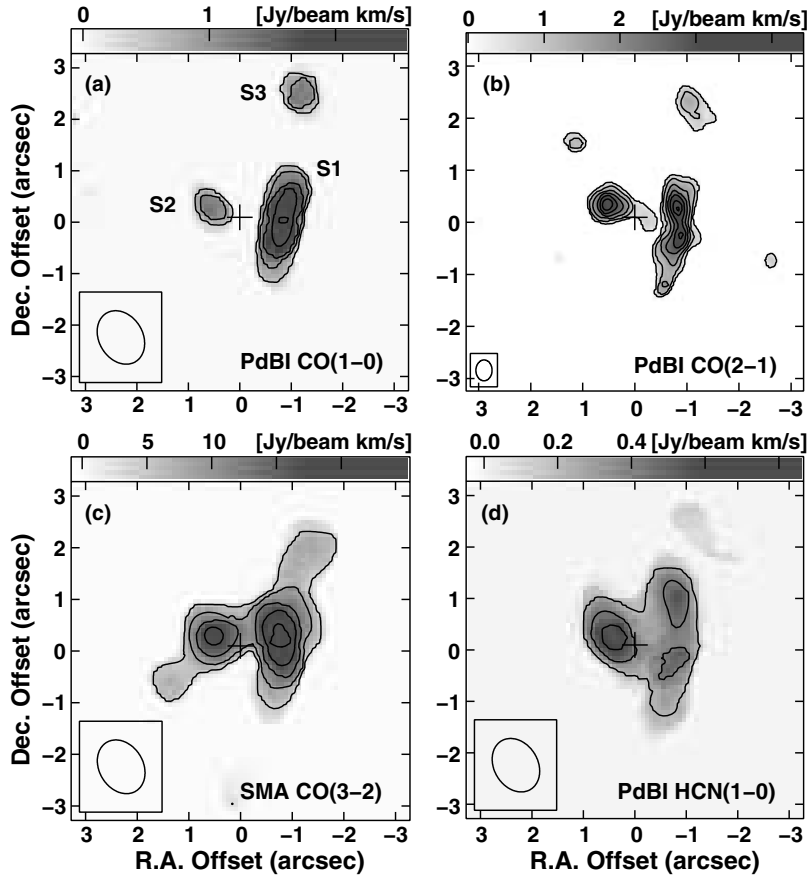[9] http://www.cfa.harvard.edu/~cqi/mircook.html

Figure 1. Integrated intensity maps of (a) CO(1–0), (b) CO(2–1), (c) CO(3–2), and (d) HCN(1–0) lines toward the central $\pm 3''$ (± 100 pc) of M51 (the CO $J = 2$–1 image is from Matsushita et al. 2007). The uv coverages and the beam sizes ($1\overset{''}{.}10 \times 0\overset{''}{.}85$, P.A. $= 31°$) are matched, except the CO(2–1) line map ($0\overset{''}{.}40 \times 0\overset{''}{.}31$, P.A. $= 0°$). The central cross in each map displays the location of the type 2 Seyfert nucleus determined from the peak of the 8.4 GHz radio continuum peak position of R.A. $= 13^{\rm h}29^{\rm m}52\overset{\rm s}{.}7101$ and decl. $= 47°11'42\overset{''}{.}696$ (Hagiwara et al. 2001; Bradley et al. 2004). In (a), three molecular gas clumps have been labeled in the same manner as in Scoville et al. (1998). Contour levels are as follows: (a) 2, 4, 6, 8, and 10×0.248 Jy beam^{-1} km s^{-1}; (b) 1, 3, 5, 7, 9, and 11×0.334 Jy beam^{-1} km s^{-1}; (c) 2, 4, 6, 8, and 10×2.21 Jy beam^{-1} km s^{-1}; (d) 2, 4, and 6×0.109 Jy beam^{-1} km s^{-1}.

After converting the integrated intensity maps of the CO(1–0) and HCN(1–0) lines in Figure 1 into brightness temperature maps, we made the HCN(1–0)/CO(1–0) brightness temperature ratio map in Figure 5 overlaid on the VLA 6 cm continuum map (Crane & van der Hulst 1992). All the molecular gas clumps show the HCN/CO ratios of more than 0.1, and the clumps closer in projection either to the AGN or to the jet tend to have higher ratios. Indeed, the highest ratio of more than 2.0 is located at the AGN (western) side of clump S2. More interestingly, all the eastern side of clump S1 has higher ratio of ∼1.0 than the western side of ∼0.3–0.5, and this side is where the radio jets are running through, which can be clearly seen in Figure 5.

The average ratios of clumps S1, S2, and S3 are calculated as 0.6, 1.5, and 0.3, respectively. On the other hand, since the CO(1–0) emission totally lacks at the nucleus (see Figure 1(a)), the HCN/CO ratio at the nucleus cannot be calculated in the ratio map. But since the HCN(1–0) emission does exist at the nucleus with the integrated intensity of 0.422 Jy beam^{-1} km s^{-1}, the lower limit of the HCN/CO brightness temperature ratio at the nucleus can be calculated as >0.96 using the 3σ upper limit of CO of 0.744 Jy beam^{-1} km s^{-1}. This is also true in the channel map at the velocity of 480 km s^{-1}; in Figure 3, no clear emission in CO(1–0) toward the nucleus with 1σ noise level of 0.45 K, while HCN(1–0) is detected with 1.5 K (∼5σ).

The radial tendency of the HCN/CO ratio is more clearly seen in the radial ratio plot. Figure 6(a) plots the radial integrated

intensity distributions of HCN(1–0) and CO(1–0) in units of K km s^{-1}. It is obvious that the HCN(1–0) emission is centrally concentrated, while the CO(1–0) emission exhibits deficiency at the nucleus. From these two radial distributions, we made the radial HCN(1–0)/CO(1–0) integrated intensity ratio plot in Figure 6(b). This figure clearly displays that the HCN/CO ratio is higher at the nucleus and decreases monotonically as the distance from the nucleus increases out to ∼$1\overset{''}{.}25$.

As mentioned in Section 2.1, we did not detect the HCO$^+$(1–0) and HNC(1–0) lines and therefore the maps for these lines are not presented in this paper. The brightness temperature ratios for both HCN(1–0)/HCO$^+$(1–0) and HCN(1–0)/HNC(1–0) are therefore >4.3 using 3σ upper limits for these non-detected lines.

4. DISCUSSION

4.1. High HCN/CO Ratios at the Nucleus and Outflowing Gas

Our high spatial resolution molecular gas images toward the Seyfert 2 nucleus of M51 clearly exhibit higher HCN(1–0)/CO(1–0) ratios in the molecular gas clumps located close to the AGN than those in other galaxies; the jet-entrained molecular gas clump (clump S1; projected distance of ∼30 pc from the nucleus) has an averaged HCN/CO ratio of 0.6, and the nearest clump from the AGN (clump S2; projected distance < 20 pc) a
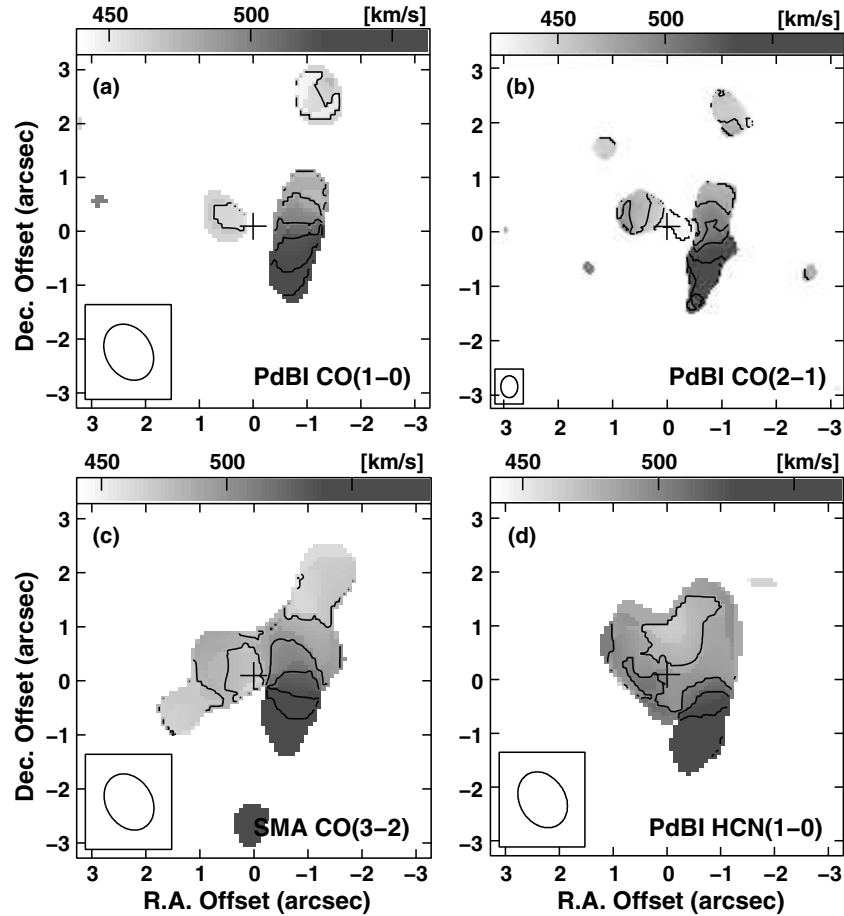
Figure 2. Intensity-weighted velocity field maps of (a) CO(1–0), (b) CO(2–1), (c) CO(3–2), and (d) HCN(1–0) lines toward the central ±3″ of M51 (the CO $J =$ 2–1 image is from Matsushita et al. 2007). Contour levels are as follows: (a) 460, 480, 500,..., 560 km s^{-1}; (b) 440, 460, 480,..., 540 km s^{-1}; (c) 460, 480, 500,..., 560 km s^{-1}; (d) 480, 500, 520, 540, and 560 km s^{-1}. Other information is the same as in Figure 1.

ratio of 1.5. Clump S3, which is located farthest from the AGN, has a ratio of 0.3.

In normal and starburst galaxies, the HCN(1–0)/CO(1–0) ratios are <0.3 (e.g., Solomon et al. 1992; Helfer & Blitz 1993; Aalto et al. 1995; Sorai et al. 2002; Gao & Solomon 2004; Kohno et al. 2008a; Matsushita et al. 2010). The ratios in our Galaxy and M31 are also low, around 0.01–0.03 for Giant Molecular Clouds (GMCs) in the galactic disks (Helfer & Blitz 1997; Brouillet et al. 2005), and up to ~0.15 at the Galactic center (Jackson et al. 1996). The ratios can be up to ~0.6 for the case of molecular gas located around Seyfert nuclei (e.g., Kohno et al. 2008a; Krips et al. 2007, 2011). Based on these values, the averaged HCN/CO ratio of clump S1 is similar to those of other Seyfert galaxies, and that of clump S3 is at the high end of normal or starburst galaxies. Clump S2 is exceptional; the HCN intensity is brighter than that of CO, and this has never been observed in other galaxies in the past.

4.2. Shocked Molecular Gas Outflow along the Radio Jets

As shown in Section 3 and in Figure 5, the S1 clump shows a high HCN/CO ratio of around unity only at the side where the radio jets overlap. In addition, this clump is known to be an outflow that is entrained by the radio jets (Matsushita et al. 2007). Such a high ratio has been observed at shocked regions of molecular outflows from young stellar objects in our Galaxy. Umemoto et al. (1992) observed a highly collimated outflow in the dark cloud L1157 with the ^{12}CO(1–0), ^{13}CO(1–0), and

HCN(1–0) lines. In their ^{12}CO spectrum, two (narrow and broad) components can be seen, which are tracing quiescent and outflowing gas, respectively. In the ^{13}CO spectrum, only a narrow component has been detected, but on the contrary, only a broad component has been detected in the HCN spectrum. Using their data, we derive the line ratios with assuming that the HCN emission is only from the outflow component and the ^{13}CO emission from quiescent component. For the ^{12}CO line, we fit a Gaussian to each component to derive the integrated intensity. We integrate all the hyperfine components of the HCN line, since our M51 data cannot distinguish these lines. From these data, we calculated the HCN/^{12}CO and HCN/^{13}CO ratios for the outflowing (shocked) gas as 0.9 and >260 (using 3σ upper limit for the ^{13}CO data), respectively. Interferometric HCN and ^{12}CO line observations of the Orion-KL high velocity outflow (Wright et al. 1996) also show high HCN/^{12}CO ratios ranging between 0.4–0.5. The ratios in the Orion-KL outflow is lower than that in the L1157 outflow, possibly due to more complex nature (and therefore larger contamination) in the massive star forming regions than in the low mass star forming regions.

The ratio and the condition of clump S1, especially the side close to the radio jets, is very similar to that of the outflowing (shocked) molecular gas in L1157. This strongly supports the idea that the high HCN/CO ratio along the radio jets in M51 is caused by the strong interaction (i.e., shock) between the jets and the outflowing molecular gas. Furthermore, it is worth mentioning that the averaged HCN/CO ratio of 0.6 is very
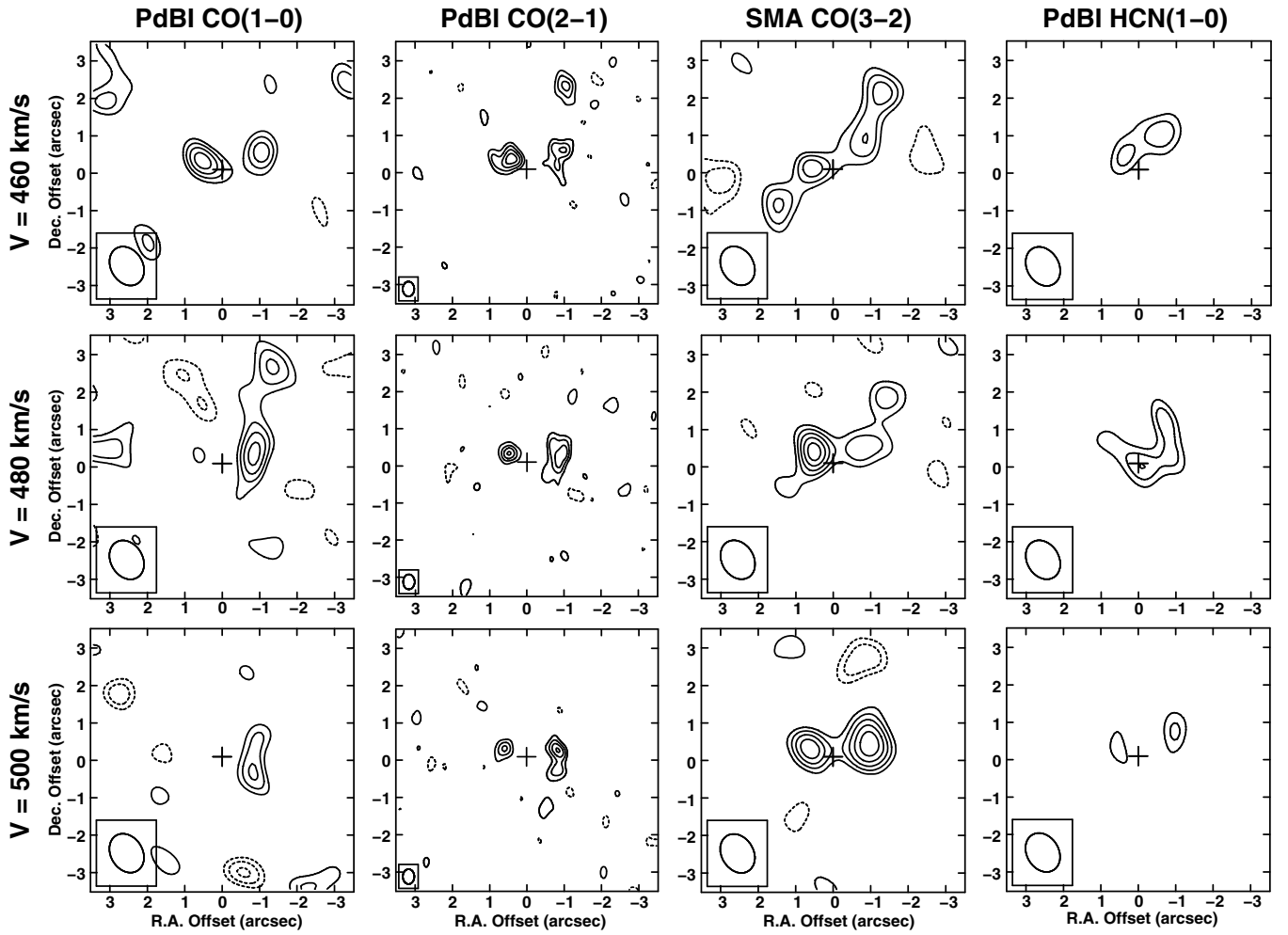
Figure 3. Central $\pm 3''$ channel maps between the velocity range of 480 ± 20 km s^{-1} (i.e., systemic velocity channel map and one channel before and after). First to fourth columns are the CO(1–0), CO(2–1), CO(3–2), and HCN(1–0) lines, respectively. First, second, and third rows are the channel maps at the velocities of 460, 480, and 500 km s^{-1}, respectively. Contour levels are as follows: CO(1–0): -4, -3, 3, 4, 5, and $6 \times 1\sigma$ ($= 4.6$ mJy beam$^{-1} = 0.45$ K); CO(2–1): -3, 3, 5, 7, and $9 \times 1\sigma$ ($= 5.2$ mJy beam$^{-1} = 0.96$ K); CO(3–2): -3, 3, 4, 5, 6, and $7 \times 1\sigma$ ($= 39.7$ mJy beam$^{-1} = 0.43$ K). HCN(1–0); -3, 3, 4, and $5 \times 1\sigma$ ($= 1.9$ mJy beam$^{-1} = 0.31$ K). Note that there was no positive or negative noise more than 3σ in the HCN(1–0) map. See the Figure 1 caption for other information.

similar to the dense molecular gas outflow observed toward Mrk 231 of ~ 0.6 (Aalto et al. 2012). Since their spatial resolution of ~ 1.2 kpc is lower than ours, it is possible that the actual HCN/CO ratio in Mrk 231 is higher.

4.3. Infrared Pumping with Weak Maser at Circumnuclear Molecular Gas?

Clump S2 shows an extremely high HCN/CO ratio of 1.5 on average, and more than 2 at the nucleus as shown in Figure 6. As mentioned above, such high ratios have not been observed in extragalactic molecular gas, but observed in molecular gas around asymptotic giant branch (AGB) stars.

We observed the high mass-loss carbon AGB stars, IRC+10216, with ^{12}CO(1–0), ^{13}CO(1–0), and HCN(1–0) for the intensity calibrations of our past observations (see Matsushita et al. 2010 for details). The resultant ^{12}CO/^{13}CO, HCN/^{12}CO, and HCN/^{13}CO integrated intensity ratios are ~ 11, 1.3, and 15, respectively. Note again that we integrate all the HCN hyperfine lines for this calculation. The high HCN/^{12}CO and HCN/^{13}CO ratios are due to the infrared (IR) pumping (Dinh-V-Trung & Nguyen-Q-Rieu 2000).

This result suggests that the extremely high HCN/CO ratio can be due to the IR pumping. In the following subsections,

we discuss what is the possible excitation mechanism for clump S2.

4.3.1. Excitation Mechanisms of the HCN Emission: I. LTE/Non-LTE Conditions

We start by assuming that both molecules are excited solely by collisions with H$_2$ molecules, which is typically the case in Galactic GMCs. The opacity ratio under the local thermal equilibrium (LTE) can be expressed as

$$\frac{\tau_{\mathrm{HCN(1-0)}}}{\tau_{\mathrm{CO(1-0)}}} = \frac{f_{\mathrm{HCN}}}{f_{\mathrm{CO}}} \left(\frac{\mu_{\mathrm{HCN}}}{\mu_{\mathrm{CO}}}\right)^2 \frac{B_{\mathrm{HCN}}}{B_{\mathrm{CO}}} \frac{[\mathrm{HCN}]}{[\mathrm{CO}]}$$
$$\times \frac{1 - \exp(-h\nu_{\mathrm{HCN(1-0)}}/kT)}{1 - \exp(-h\nu_{\mathrm{CO(1-0)}}/kT)}, \quad (1)$$

where f is the filling factor, μ is the dipole moment, B is the rotational constant, h is the Planck constant, ν is the rotational transition frequency, and k is the Boltzmann constant. The HCN and CO molecular abundances relative to H$_2$ are expressed as [HCN] and [CO], respectively. Adopting $f_{\mathrm{HCN}} = f_{\mathrm{CO}}$, which is already an extreme case compared to the Galactic GMCs where $f_{\mathrm{HCN}} \ll f_{\mathrm{CO}}$, $\mu_{\mathrm{HCN}} = 2.984$, $\mu_{\mathrm{CO}} = 0.112$,
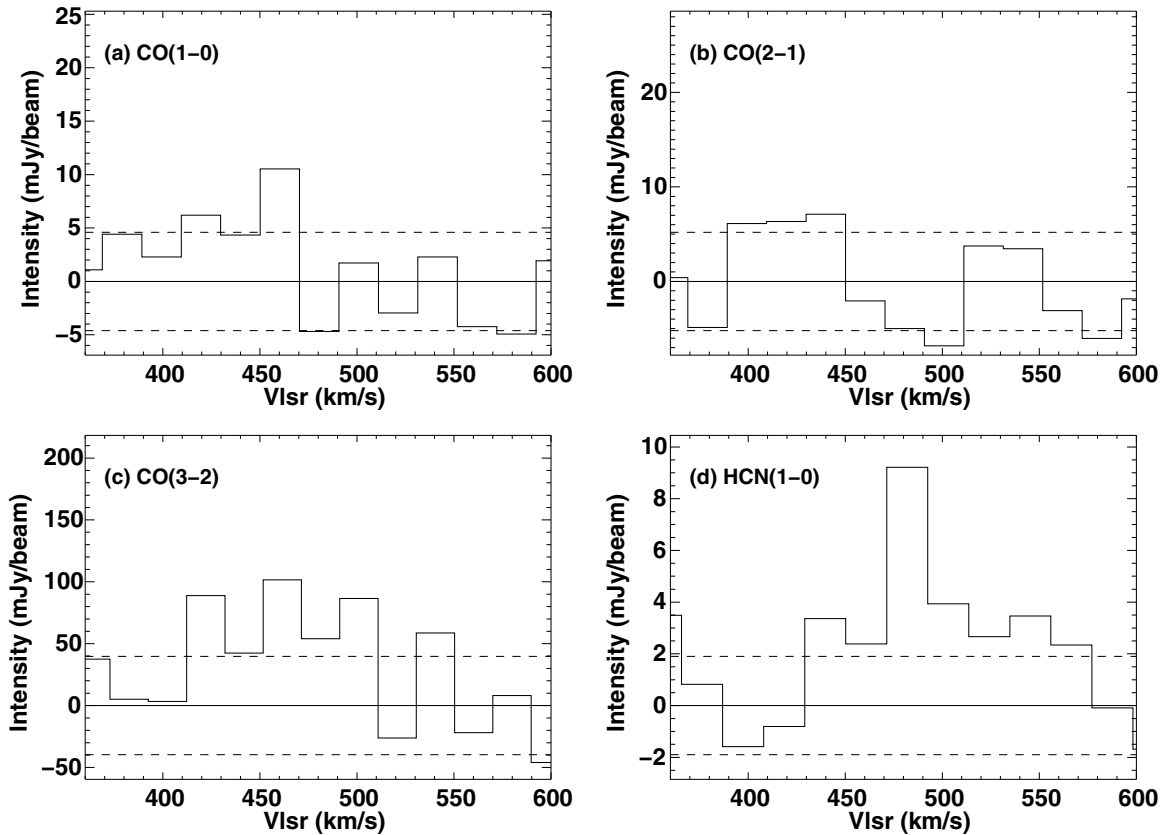
Figure 4. Spectra toward the M51 nucleus for (a) CO(1–0), (b) CO(2–1), (c) CO(3–2), and (d) HCN(1–0) lines. The spectra have been taken at the position of the nucleus with the spatial resolution the same as the beam sizes. The nuclear position and the beam sizes are mentioned in the caption of Figure 1. Horizontal dashed lines in each plot are $\pm 1\sigma$ of each data set (see the caption of Figure 1 for the values). All the CO lines exhibit at most $\sim 2\sigma$ peaks, but the HCN(1–0) line only at the velocity channel of $480\,\mathrm{km\,s^{-1}}$, which includes the systemic velocity of $471.7 \pm 0.3\,\mathrm{km\,s^{-1}}$ (Shetty et al. 2007), shows a $\sim 5\sigma$ peak.

B_{HCN} = 44.316 GHz, B_{CO} = 57.636 GHz, ν_{HCN} = 88.631 GHz, ν_{CO} = 115.271 GHz, [HCN] = 2×10^{-8} (Irvine et al. 1987), and [CO] = 5×10^{-5}, the opacity ratio can be calculated as $\tau_{\mathrm{HCN(1-0)}}/\tau_{\mathrm{CO(1-0)}} \sim 0.18 \pm 0.01$ under a large range of molecular gas temperature condition ($T \sim 3$–$1000\,\mathrm{K}$). The brightness temperature ratio can therefore be expressed as

$$\frac{T_{\mathrm{HCN(1-0)}}}{T_{\mathrm{CO(1-0)}}} = \frac{1 - \exp(-\tau_{\mathrm{HCN}})}{1 - \exp(-\tau_{\mathrm{CO}})}$$
$$\sim \frac{1 - \exp(-0.18\tau_{\mathrm{CO}})}{1 - \exp(-\tau_{\mathrm{CO}})}, \qquad (2)$$

and this ratio ranges between 0.18 (optically thin limit) and 1 (optically thick limit), which cannot realize HCN(1–0)/CO(1–0) > 1.

If f_{HCN} is ~ 10 times larger than f_{CO}, then it is possible to obtain the observed ratio, but it is physically unlikely; the critical density of the HCN molecule is more than an order of magnitude larger than that of the CO molecule, so that wherever the HCN molecules can emit, the CO molecules can also emit, and f_{HCN} cannot be larger than f_{CO}. A simple way to reproduce the observed HCN/CO ratio would be if the [HCN]/[CO] abundance ratio is increased by a factor of ~ 10. In either case, the CO emission should be optically thin. This is also true even for the non-LTE radiation transfer modeling using the large-velocity-gradient (LVG) approximation; without changing the HCN abundance, the HCN/CO ratio can be at most around unity under very limited temperature or density range (see Section 4.3.2 and Figure 7(c)).

4.3.2. Excitation Mechanisms of the HCN Emission: II. Infrared Pumping

In addition to the collisional excitation, here we also consider the possibility of IR radiative pumping (Morris 1975; Carrol & Goldsmith 1981; Deguchi & Uyemura 1984), since this mechanism can enhance the HCN intensity as mentioned for the case of IRC+10216 in Section 4.3. This mechanism is to pump the population of a rotational level to higher levels via vibrational transitions; in a strong IR radiation field, some molecules that have vibrational transitions at an IR wavelength will be pumped to higher *vibrational* levels and radiate back to lower levels, but to higher *rotational* levels than before. This process increases the population at higher rotational levels and therefore makes the rotational transition emission stronger than general molecular clouds (no strong IR field), which only have collisional pumping. This is particularly relevant when a luminous source is present (e.g., AGN) in the background, such that optical/UV radiation is absorbed by dust and reradiated in the IR. The vibrational transition of HCN molecule is at $14\,\mu\mathrm{m}$, where the radiation from warm dust irradiated by AGNs is strong, and therefore this is one of the possible mechanisms to explain the high HCN/CO ratio toward AGNs. The absorption line of the HCN $14\,\mu\mathrm{m}$ transition can be seen in several IR luminous galaxies (Lahuis et al. 2007; Farrah et al. 2007). Recent interferometric observations toward those galaxies have indeed displayed vibrationally excited HCN lines toward their IR luminous nuclei (Salter et al. 2008; Sakamoto et al. 2010; Imanishi et al. 2013).
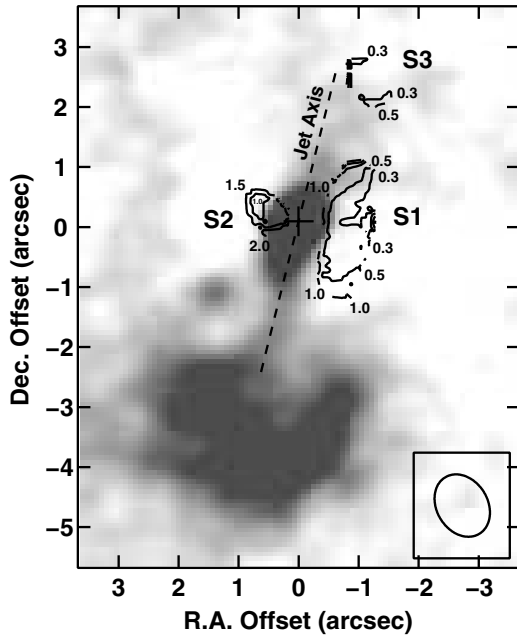
Figure 5. HCN(1–0)/CO(1–0) brightness temperature ratio map (contours) overlaid on the VLA 6 cm radio continuum image (grayscale; Crane & van der Hulst 1992). Contour levels are presented in the map. The dashed line shows the radio jet axis (P.A. = 166°; Bradley et al. 2004), and the continuum image is enhanced to show the weak jet emission elongated toward southeast, and connected to the bow-shock emission at southeast of this image. The average ratios for clumps S1, S2, and S3 are calculated as 0.6, 1.5, and 0.3, respectively. S1 is clearly elongated along this jet emission (see also Matsushita et al. 2007), and the higher ratio regions are concentrated where S1 and the jet overlap. S2 mostly overlaps with the jet emission and has high ratio overall, but is higher toward the Seyfert 2 nucleus. The cross at the center is the same as in Figure 1.

To check whether IR pumping of HCN can occur near the nucleus, we need to estimate the radiative excitation in this region. The condition for the IR pumping to be effective is when the probability of the HCN $v = 0 - 1$ vibrational transition absorption at 14 μm, $B_{v=0-1}I_{14\mu m}$ (s^{-1}), is larger than that of the HCN $J = 1$–0 rotational transition spontaneous emission, $A_{J=1-0}$ (s^{-1}), namely,

$$B_{v=0-1}I_{14\mu m} \geqslant A_{J=1-0}, \tag{3}$$

where $I_{14\mu m}$ is the average intensity of the radiation field at 14 μm. This equation can be re-written as

$$\frac{c^2}{2h\nu^3}A_{v=1-0}I_{14\mu m} \geqslant A_{J=1-0}, \tag{4}$$

where c is the speed of light, h is the Planck constant, and ν is the frequency. We use $A_{v=1-0} = 2.23\,\mathrm{s}^{-1}$ (Harris et al. 2006) from the GEISA spectroscopic database (Jacquinet-Husson et al. 2011) and $A_{J=1-0} = 2.41 \times 10^{-5}\,\mathrm{s}^{-1}$ (Dumouchel et al. 2010) from RADEX (Van der Tak et al. 2007) for this calculation.

To estimate the radiation field at 14 μm around the nucleus of M51, we use the recent high resolution images taken with the photometric bands S11 (11 μm) and L15 (15 μm) of the *AKARI* Infrared Camera (Egusa et al. 2013). Both images show a point-like source at the nucleus of M51 at a spatial resolution of 7″4, and well separated from the surrounding spiral arms (i.e., no contamination from the emission of the spiral arms; see Figure 2 of Egusa et al. 2013). We therefore assume that the point-like emission at the nucleus of M51 in these images originates from the compact Seyfert 2 nucleus. The flux densities

of the nuclear emission at S11 and L15 are 3.7×10^{-2} Jy and 6.4×10^{-2} Jy, respectively. With linear interpolation between S11 and L15 flux densities, we estimate a 14 μm flux density, $S_{14\mu m}$, of 5.7×10^{-2} Jy.

$I_{14\mu m}$ can be calculated using $S_{14\mu m}$ as

$$I_{14\mu m} = \frac{S_{14\mu m}}{\Omega_{14\mu m}}, \tag{5}$$

where $\Omega_{14\mu m}$ is the solid angle of the source at 14 μm. Since the compact infrared nuclear source of M51 has not been resolved so far, we adopt the size of the infrared source as a few (2–3) pc, which is the same as that of the thick dust disk observed toward the nucleus of the prototypical Seyfert 2 galaxy NGC 1068 (Jaffe et al. 2004). Substituting the above values into Equations (5) and (4), the left-hand side of the Equation (4) is calculated as $(3.3–9.2) \times 10^{-5}\,\mathrm{s}^{-1}$, which is larger than the right-hand side of the equation of $2.41 \times 10^{-5}\,\mathrm{s}^{-1}$. This indicates that IR pumping can occur in the molecular gas surrounding the Seyfert 2 nucleus of M51.

We then included the infrared pumping effect in our LVG calculations. We use the above calculated 14 μm intensity for the radiation coming from the background infrared source. Here, we adopt the infrared source size of 3 pc. We also assume that the molecular gas has a temperature of 100 K. Note that in general higher molecular gas temperature induces more collision, and therefore decreases the effect of infrared pumping. But under the high temperature condition, the effect of infrared pumping to lower transitions is insensitive to changes in the molecular gas temperature, since most of population is at higher transitions; a factor of a few change in temperature gives almost no difference in the calculation results.

In the first calculation, we use the H_2 column density per velocity of 1×10^{21} cm^{-2}, which corresponds to the H_2 column density toward the nucleus of M51 (6.2×10^{21} cm^{-2}; Matsushita et al. 2007) divided by the typical velocity width of the extragalactic molecular clouds of 6–8 km s^{-1} (Combes & Becquaert 1997). We also assume that the column densities per velocity for CO and HCN, N_{CO}/dv and N_{HCN}/dv, are 5×10^{16} cm^{-2} (km s^{-1})$^{-1}$ and 3×10^{13} cm^{-2} (km s^{-1})$^{-1}$, respectively. These column densities for CO and HCN correspond to the normal abundance ratio mentioned in Section 4.3.1 relative to the H_2 column density mentioned above. The results for the brightness temperatures of CO (black curves) and HCN (red curves) lines are shown in Figure 7(a), with the comparison of the results without infrared pumping (Figure 7(c)). As can be seen, using the normal abundance of HCN and CO, the HCN(1–0)/CO(1–0) ratio of at most about unity can be realized under very limited condition of $n_{H_2} \sim 10^{5–6}$ cm^{-3}, but cannot realize HCN(1–0)/CO(1–0) >2 both with and without infrared pumping.

We then repeated the calculations by increasing the HCN abundance by an order of magnitude, namely, changing N_{HCN}/dv to 3×10^{14} cm^{-2} (km s^{-1})$^{-1}$. The calculation results are displayed in Figure 7(b), with the comparison of the results without infrared pumping (Figure 7(d)). In both cases, a high HCN(1–0)/CO(1–0) ratio of >2 can be obtained at dense condition ($n_{H_2} > 10^5$ cm^{-3}). On the other hand, when including infrared pumping, HCN(1–0)/CO(1–0) >2 can also be obtained even at low density condition, namely, it is possible at a large density range.

Note that with the H_2 column density per velocity we used, the CO brightness temperatures, especially $J = 1$–0, are much lower than the assumed molecular gas temperature of 100 K,
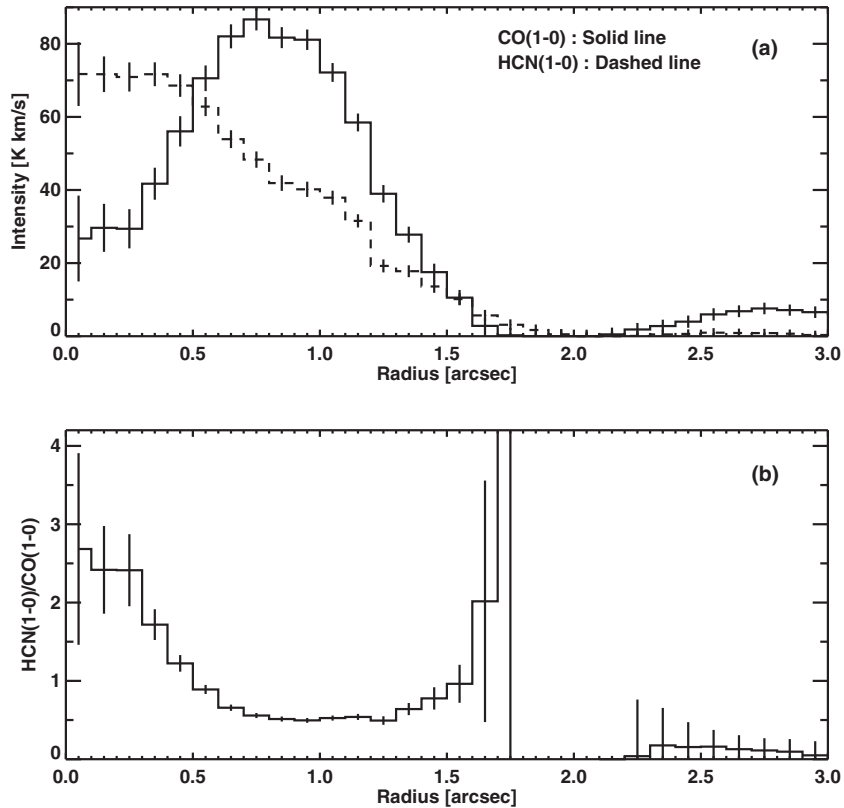
Figure 6. (a) Central $3''$ radial intensity distributions of the CO(1–0) (solid line) and HCN(1–0) (dashed line) emission derived from the integrated intensity maps in Figure 1 after converted into brightness temperature scale. (b) Central $3''$ HCN/CO integrated intensity ratio distribution. The uv coverages are matched between these two lines.

since CO is already thermalized and the population is at higher-J transitions, which makes the lower-J lines optically thin and therefore low brightness temperatures. This is consistent with the non-detection of the CO lines toward the nucleus under the current noise level of $\sim$2–3 K at 3σ upper limit (see Figure 3) and the detection of the HCN(1–0) line.

In summary, infrared pumping does not need to be invoked to realize a high HCN(1–0)/CO(1–0) ratio of >2, but with infrared pumping, it is easier to realize. Since this is not conclusive only with the LVG calculations, we discuss the possibility of infrared pumping with other observational results in the next subsection.

4.3.3. Possible Causes of High HCN Abundance

Based on the radiative transfer calculations above, it is necessary to have a high HCN abundance to realize a high HCN(1–0)/CO(1–0) ratio. There are several ways in which the HCN abundance may be enhanced. One possibility is due to high X-ray radiation from AGNs. Since X-ray radiation penetrates much deeper and denser regions than UV radiation, the chemical reactions exhibits different pathways compared with photodissociated region. The molecular gas region that is irradiated by X-ray is called X-ray-dominated region (XDR; Maloney et al. 1996), and some radiative transfer calculations of XDR succeeded to enhance the HCN abundance (Lepp & Dargarno 1996; Lintott & Viti 2006), but some do not (Meijerink & Spaans 2005; Meijerink et al. 2007). A second possibility is energetic particles (i.e., cosmic rays) either from AGNs or radio jets. This possibility, however, reduces the HCN and HNC abundances, and increases the HCO$^+$ abundance (Bayet et al. 2010), which do not match with our results. Another possibility is the high temperature gas phase chemistry as

recently suggested by Harada et al. (2010, 2013). This radiative transfer calculation includes the time-dependent interstellar chemical gas-phase reaction network, so that this calculation gives resultant molecular gas abundances under strong heating by X-ray irradiation. The calculation results show high HCN abundance, which matches with our observations. Furthermore, the HNC abundance increase is an order of magnitude less than that for the HCN abundance, and the HCO$^+$ abundance shows decrement under this model, which again matches with our results of non-detection for the HCO$^+$(1–0) and HNC(1–0) lines. Indeed, the HCO$^+$ vibrational absorption line at $12\,\mu$m has not been detected toward the luminous infrared galaxies from which the HCN vibrational absorption line at $14\,\mu$m has been detected (Imanishi et al. 2010). Since the HCO$^+$ vibrational transition is located at a similar wavelength and has a similar Einstein coefficient as that of the HCN vibrational transition, non-detection of the HCO$^+$ absorption line suggests that the HCN abundance has enhanced compared to that of the HCO$^+$, consistent with this model. In addition, high HCN/HNC abundance ratios have been observed toward active star forming cores (Goldsmith et al. 1986; Schilke et al. 1992), and low ratios in starless cores (Hirota et al. 1998) in our Galaxy, which is again consistent with this model. Our results therefore strongly support the model presented in Harada et al. (2010, 2013).

On the other hand, the radiative transfer calculation results in Section 4.3.2 cannot realize HCN(1–0)/CO(3–2) above unity even under the HCN abundance enhanced conditions; in the CO(3–2) map (Figure 3), contours at the level of 3–4σ, namely, 1.3–1.7 K, are at the nucleus, but no intensity peak has been observed as in the HCN map, if we consider the beam size. This suggests that HCN(1–0) is stronger than CO(3–2) at the
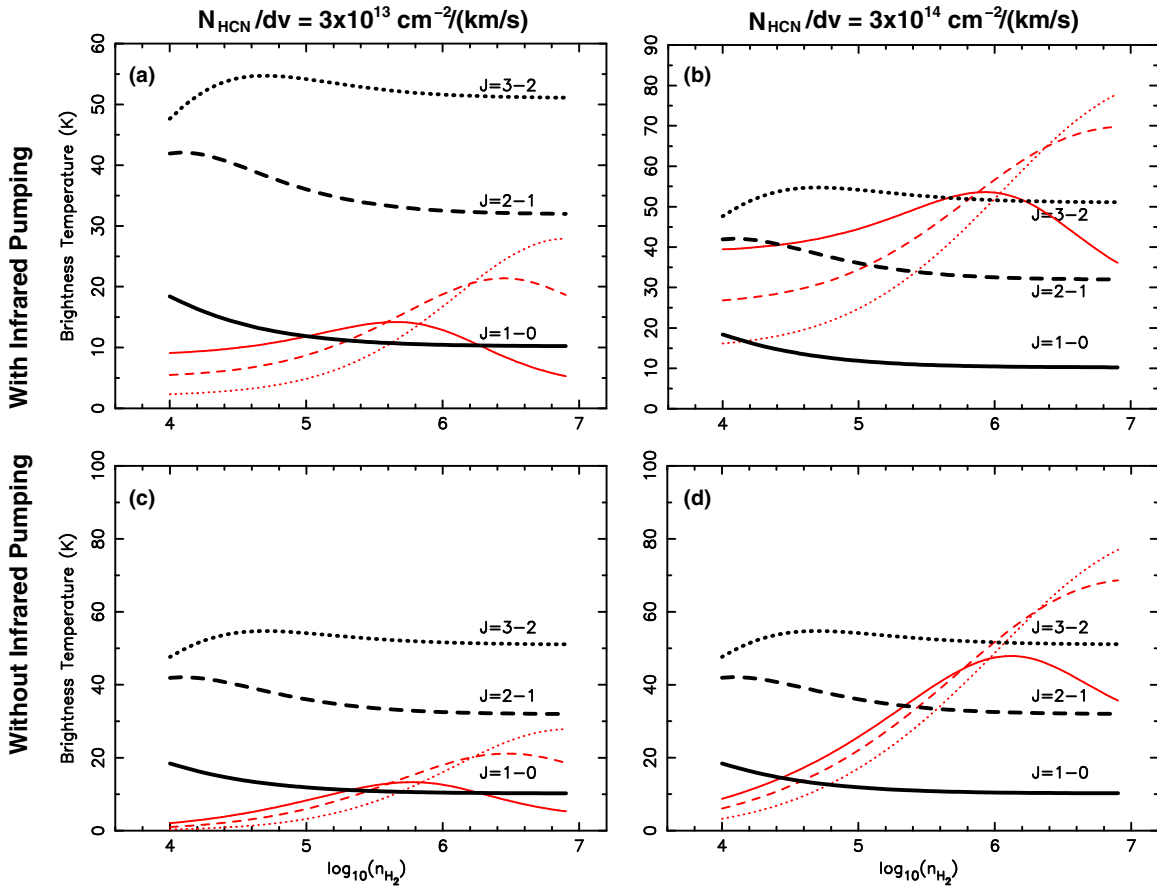
Figure 7. LVG calculation results with (upper row plots) and without (bottom row plots) IR pumping. We adopted the kinetic temperature of molecular gas as 100 K. Plots are brightness temperatures (kelvin) of CO (black lines) and HCN (red lines) as a function of H_2 number density (cm^{-3}). Solid, dashed, and dotted lines are the results for $J = 1-0$, 2–1, and 3–2 transitions, respectively. (a) Result with N_{HCN}/dv of 3×10^{13} cm^{-2} (km s^{-1})$^{-1}$ and with IR pumping. (b) Result with N_{HCN}/dv of 3×10^{14} cm^{-2} (km s^{-1})$^{-1}$ and with IR pumping. (c) Result with N_{HCN}/dv of 3×10^{13} cm^{-2} (km s^{-1})$^{-1}$ but without IR pumping. (d) Result with N_{HCN}/dv of 3×10^{14} cm^{-2} (km s^{-1})$^{-1}$ but without IR pumping.

nucleus, which is inconsistent with the calculation results in Figure 7. One possible mechanism to make the HCN(1–0) emission strong is weak HCN masing. The infrared pumping can invert the population at the HCN(1–0) transition and possible to produce the maser emission at this transition (Dinh-V-Trung & Nguyen-Q-Rieu 2000). The HCN(1–0) masers have indeed been observed toward various carbon stars (Izumiura et al. 1987, 1995; Olofsson et al. 1993). Under this excitation condition, and if the HCN molecule is distributed as an edge-on torus or disk that is similar to the water maser disk in NGC 4258 (Miyoshi et al. 1995), it is possible to create HCN maser emission at the systemic velocity. This matches well with the strong HCN(1–0) nuclear emission only at the systemic velocity channel (Figures 3 and 4). A similar explanation has been discussed for the strong spike in the HNC(3–2) emission for the western nucleus of Arp 220 (Aalto et al. 2009), although our observation has not detected any HNC emission, probably due to the high temperature gas phase chemistry in our case, as mentioned above.

Our results therefore suggest that there is a compact dense molecular gas in front of the type 2 AGN in M51 that cannot be resolved in our spatial resolution of $\sim$1″ ($\sim$ 34 pc). This component can be the obscuring material for the type 2 nucleus of M51; assume this component has a size of $\sim$1 pc (i.e., much smaller than the spatial resolution of our observations) along the line of sight and a density of $\sim$10^6 cm^{-3} (i.e., consistent with the radiative transfer calculation results in Section 4.3.2), then

the column density along the line of sight will be calculated as $\sim$3 × 10^{24} cm^{-2}. This value is consistent with the column density of $\sim$5.6 × 10^{24} cm^{-2} for the absorption material in front of the nuclear X-ray source (i.e., AGN) of M51 (Fukazawa et al. 2001). It is highly required to observe HCN lines with $\ll$1″ resolution toward M51 to directly image the obscuring material in front of the AGN, which may give us knowledge about the still-unknown obscuring and feeding mechanisms of AGNs.

5. SUMMARY

Our newly obtained $\sim$1″ ($\sim$34 pc) resolution HCN(1–0) image toward the Seyfert 2 nucleus of M51 (NGC 5194) revealed the following results.

1. The overall HCN(1–0) distribution and kinematics are similar to those of the CO lines. Since it is known that the kinematics derived from the CO lines indicates the jet-entrained nature, this similarity indicates that the dense gas is also entrained by the jets and outflowing from the AGN.

2. HCN(1–0)/CO(1–0) brightness temperature ratio is strongly enhanced along the jets with the value around unity, and the value is similar to that of the shocked gas in the outflows from young stellar objects in our Galaxy, suggesting that the HCN enhancement along the jets are highly related to shock.

3. A strong HCN(1–0) emission has been detected toward the nucleus only at the systemic velocity channel. No CO

emission has been detected at this region and at this velocity, and therefore the ratio turned out to be more than 2. To realize this high ratio, it is suggested from our radiative transfer model that weak HCN maser triggered by the infrared pumping with HCN abundance enhancement is the possible mechanism. The most plausible configuration for emitting the HCN maser is a rotating edge-on dense molecular gas disk or torus around the AGN, similar to the water maser disks in other Seyfert 2 galaxies. If this disk or torus has the size of ~ 1 pc and the density of $\sim 10^6$ cm^{-2}, then it is possible to explain the nuclear obscuration for this type 2 AGN in M51.

4. Cause of the high HCN abundance can be due to high temperature gas phase chemistry. Non-detection of the HCO$^+$(1–0) and HNC(1–0) lines in our observations also support this model.

REFERENCES

Aalto, S., Booth, R. S., Black, J. H., & Johansson, L. E. B. 1995, A&A, 300, 369
Aalto, S., Garcia-Burillo, S., Muller, S., et al. 2012, A&A, 537, A44
Aalto, S., Wilner, D., Spaans, M., et al. 2009, A&A, 493, 481
Antonucci, R. R. J. 1993, ARA&A, 31, 473
Bayet, E., Hartquist, T. W., Viti, S., Williams, D. A., & Bell, T. A. 2010, A&A, 521, A16
Bradley, L. D., Kaiser, M. E., & Baan, W. A. 2004, ApJ, 603, 463
Brouillet, N., Muller, S., Herpin, F., Braine, J., & Jacq, T. 2005, A&A, 429, 153
Carrol, T. J., & Goldsmith, P. F. 1981, ApJ, 245, 891
Combes, F., & Becquaert, J.-F. 1997, A&A, 326, 554
Combes, F., García-Burillo, S., Casasola, V., et al. 2013, A&A, 558, A124
Crane, P. C., & van der Hulst, J. M. 1992, AJ, 103, 1146
Davies, R. I., Maciejewski, W., Hicks, E. K. S., et al. 2009, ApJ, 702, 114
Deguchi, S., & Uyemura, M. 1984, ApJ, 285, 153
Dinh-V-Trung, & Nguyen-Q-Rieu 2000, A&A, 361, 601
Dumouchel, F., Faure, A., & Lique, F. 2010, MNRAS, 406, 2488
Egusa, F., Wada, T., Sakon, I., et al. 2013, ApJ, 778, 1
Farrah, D., Bernard-Salas, J., Spoon, H. W. W., et al. 2007, ApJ, 667, 149
Ford, H. C., Crane, P. C., Jacoby, G. H., Lawrie, D. G., & van der Hulst, J. M. 1985, ApJ, 293, 132
Fukazawa, Y., Iyomoto, N., Kubota, A., Matsumoto, Y., & Makishima, K. 2001, A&A, 374, 73
Gao, Y., & Solomon, P. M. 2004, ApJ, 606, 271
García-Burillo, S., Combes, F., Usero, A., et al. 2014, A&A, 567, A125

Goldsmith, P. F., Irvine, W. M., Hjalmarson, A., & Ellder, J. 1986, ApJ, 310, 383
Hagiwara, Y., Henkel, C., Menten, K. M., & Nakai, N. 2001, ApJL, 560, L37
Harada, N., Herbst, E., & Wakelam, V. 2010, ApJ, 721, 1570
Harada, N., Thompson, T. A., & Herbst, E. 2013, ApJ, 765, 108
Harris, G. J., Tennyson, J., Kaminsky, B. M., Pavlenko, Ya. V., & Jones, H. R. A. 2006, MNRAS, 367, 400
Helfer, T. T., & Blitz, L. 1993, ApJ, 419, 86
Helfer, T. T., & Blitz, L. 1997, ApJ, 478, 233
Hicks, E. K. S., Davies, R. I., Malkan, M. A., et al. 2009, ApJ, 696, 448
Hirota, T., Yamamoto, S., Mikami, H., & Ohishi, M. 1998, ApJ, 503, 717
Ho, L. C., Filippenko, A. V., & Sargent, W. L. L. 1997, ApJS, 112, 315
Ho, P. T. P., Moran, J. M., & Lo, F. 2004, ApJ, 616, L1
Hsieh, P.-Y., Matsushita., S., Lim, J., Kohno, K., & Sawada-Satoh, S. 2008, ApJ, 683, 70
Imanishi, M., & Nakanishi, K. 2013, AJ, 146, 91
Imanishi, M., Nakanishi, K., Yamada, M., Tamura, Y., & Kohno, K. 2010, PASJ, 62, 201
Irvine, W. M., Goldsmith, P. F., & Hjalmarson, A. 1987, in Interstellar Process, ed. D. J. Hollenbach & H. A. Thronson (Dordrecht: Reidel), 585
Izumiura, H., Ukita, N., Kawabe, R., et al. 1987, ApJL, 323, L81
Izumiura, H., Ukita, N., & Tsuji, T. 1995, ApJ, 440, 728
Jackson, J. M., Heyer, M. H., Paglione, T. A. D., & Bolatto, A. D. 1996, ApJL, 456, L91
Jackson, J. M., Paglione, T. A. D., Ishizuki, S., & Rieu, N. Q. 1993, ApJL, 418, L13
Jacquinet-Husson, N., Crepeau, L., Armante, R., et al. 2011, JQSRT, 112, 2395
Jaffe, W., Meisenheimer, K., & Röttgering, H. J. A. 2004, Natur, 429, 47
Kohno, K., Kawabe, R., Tosaki, T., & Okumura, S. K. 1996, ApJL, 461, L29
Kohno, K., Matsushita, S., Vila-Vilaró, B., et al. 2001, in ASP Conf. Ser. 249, The Central Kiloparsec of Starbursts and AGN: The La Palma Connection, ed. J. H. Knapen et al. (San Francisco, CA: ASP), 672
Kohno, K., Muraoka, K., Hatsukade, B., et al. 2008a, in Far-Infrared Workshop 2007, ed. C. Kramer, S. Aalto, & R. Simon (EAS Publication Ser., Vol. 31; Les Ulis, France; EDP Sciences), 65
Kohno, K., Nakanishi, K., Tosaki, T., et al. 2008b, Ap&SS, 313, 279
Krips, M., Martín, S., Eckart, A., et al. 2011, ApJ, 736, 37
Krips, M., Neri, R., García-Burillo, S., et al. 2007, A&A, 468, L63
Lahuis, F., Spoon, H. W. W., Tielens, A. G. G. M., et al. 2007, ApJ, 659, 296
Lepp, S., & Dalgarno, A. 1996, A&A, 306, L21
Lintott, C., & Viti, S. 2006, ApJL, 646, L37
Maloney, P. R., Hollenbach, D. J., & Tielens, A. G. G. M. 1996, ApJ, 466, 561
Matsushita, S., Kawabe, R., Kohno, K., Tosaki, T., & Vila-Vilaró, B. 2010, PASJ, 62, 409
Matsushita, S., Kohno, K., Vila-Vilaró, B., Tosaki, T., & Kawabe, R. 1998, ApJ, 495, 267
Matsushita, S., Muller, S., & Lim, J. 2007, A&A, 468, L49
Matsushita, S., Sakamoto, K., Kuo, C.-Y., et al. 2004, ApJL, 616, L55
Meijerink, R., & Spaans, M. 2005, A&A, 436, 397
Meijerink, R., Spaans, M., & Israel, F. P. 2007, A&A, 461, 793
Miyoshi, M., Moran, J., Herrnstein, J., et al. 1995, Natur, 373, 127
Morris, M. 1975, ApJ, 197, 603
Müller Sánchez, F., Davies, R. I., Genzel, R., et al. 2009, ApJ, 691, 749
Olofsson, H., Eriksson, K., Gustafsson, B., & Carlstrom, U. 1993, ApJS, 87, 305
Sakamoto, K., Aalto, S., Evans, A. S., Wiedner, M. C., & Wilner, D. J. 2010, ApJL, 725, L228
Salter, C. J., Ghosh, T., Catinella, B., et al. 2008, AJ, 136, 389
Sani, E., Davies, R. I., Sternberg, A., et al. 2012, MNRAS, 424, 1963
Schilke, P., Walmsley, C. M., Pineau Des Forets, G., et al. 1992, A&A, 256, 595
Scoville, N. Z., Yun, M. S., Armus, L., & Ford, H. 1998, ApJL, 493, L63
Shetty, R., Vogel, S. N., Ostriker, E. C., & Teuben, P. J. 2007, ApJ, 665, 1138
Solomon, P. M., Downes, D., & Radford, S. J. E. 1992, ApJL, 387, L55
Sorai, K., Nakai, N., Kuno, N., & Nishiyama, K. 2002, PASJ, 54, 179
Takáts, K., & Vinkó, J. 2006, MNRAS, 372, 1735
Tully, R. B. 1988, Nearby Galaxies Catalog (Cambridge: Cambridge Univ. Press)
Umemoto, T., Iwata, T., Fukui, Y., et al. 1992, ApJL, 392, L83
Van der Tak, F. F. S., Black, J. H., Schöier, F. L., Jansen, D. J., & van Dishoeck, E. F. 2007, A&A, 468, 627
Wright, M. C. H., Plambeck, R. L., & Wilner, D. J. 1996, ApJ, 469, 216